Chapter 3

Magnetic phase transition and spin structure of helimagnet $NiBr_2$

3.1 Introduction

In this chapter, deals with the crystal and magnetic structure of transition metal dihalide $NiBr_2$ and experimental results that were obtained on single crystals by utilizing dc magnetometry. Special attention had been paid towards the magnetic phase diagram of helimagnet $NiBr_2$ at low temperature. The temperature dependence of magnetization (M) on single crystal $NiBr_2$ measured for various values of field applied in (a–b) basal plane. Differential magnetic susceptibility $dM(H)/dH$ vs. magnetic field (H) measured in the (a-b) basal plane for various temperatures lying in the range of 10-100 K had been extracted in order to support the magnetic phase transition in helimagnet $NiBr_2$.

Transition metal di-halides MX_2 (M = metal cation, X = halogen anion) have attracted much attention with the discovery of magnetic skyrmions [60] due to the fact that several of the MX_2 compounds display non-collinear spin structures and multiferroic behaviour [17, 67–69]. In such a system, noncollinearity of spin arises due to the presence of competing exchange interactions along with magnetic anisotropy [17, 68]. These spin triangular lattice systems are also considered as a special class of materials showing unique magnetism and ferroelectricity at nanolength scale. The multiferroic helimagnets will play a vital role in designing energy efficient data storage devices [69]. Few investigations already have been carried out to understand the microscopic source of incommensurate

ordering that responsible for helimagnetism in the spin triangular lattices of $NiBr_2$ [59, 68]. However, enhanced understandings of such phase transitions further need to be established.

$NiBr_2$ crystallizes in centrosymmetric rhombohedral $CdCl_2$ type crystal structure having space group $R\bar{3}m$ belonging to the point group D^5_{3d} [64, 67, 131–133], the respective space group leads to specific extinction conditions like $-h+k+l = 3n$ and $-h+k = 3n$ for *hkil* and *hki0* reflections. $NiBr_2$ has presented with immense renewed interest as a long-wavelength helical spin structure with improper ferroelectricity [67] and its potential to host a magnetic vortex state [134, 135]. On the other hand, the symmetry groups in which triangular lattice of helimagnet theoretically predicted to have multiple-q states, bubble and the Skyrmion Lattice under applied magnetic field [18, 60, 136], all the phenomena are associated with the helimagnetic ground state. These materials are supposed to be a potential candidate for the quest of realizing ultra dense-magnetic memory and storage devices [137, 138]. The spins are arranged ferromagnetically in the (a–b) plane and coupled the planes antiferromagnetically along the c-axis.

These materials have long been studied as one of the prototypes of antiferromagnets with a triangular spin-lattice [64, 67, 68]. The first time helimagnetic ground state in this material was experimentally observed by Day *et al.* [131] employing neutron diffraction conducted on single crystal samples. These results are in agreement with the theoretical prediction of the helimagnetic structure [139] based on the magnetic measurements and the subsequent theoretical interpretation in terms of the exchange interactions in a centrosymmetric magnet. In a helical state, spins are arranged to form the ground state helix in (a–b) basal plane. An applied magnetic field can gradually stabilize/destabilize the helical structure into a soliton lattice with an eventual incommensurate-to-commensurate phase transition into a critical ferromagnetic state field of 0.1 T and destabilized above 3 T. Manipulation of the spin spiral state with the magnetic field has generated considerable interest in this material for spintronics applications [137, 137, 138].

3.2 Crystal structure

Fig. 3.1(a) illustrates the crystal structure for triangular-lattice of $NiBr_2$ crystallizes in the prototype $CdCl_2$ layered structure with ABC stacking pattern having three $NiBr_2$ layers per unit cell, and form a layered hexagonal structure. A single rhombohedral unit cell is highlighted, and lines connect atoms to eye-guideline having lattice constants a = b=3.723 Å and c =18.340 Å. In this space group, the Ni and Br atoms are situated at the Wyckoff positions 3a (0,0,0) and 6c (0,0,z) with 3*m* and -3*m* local symmetries, respectively [64, 67, 68, 131, 133].

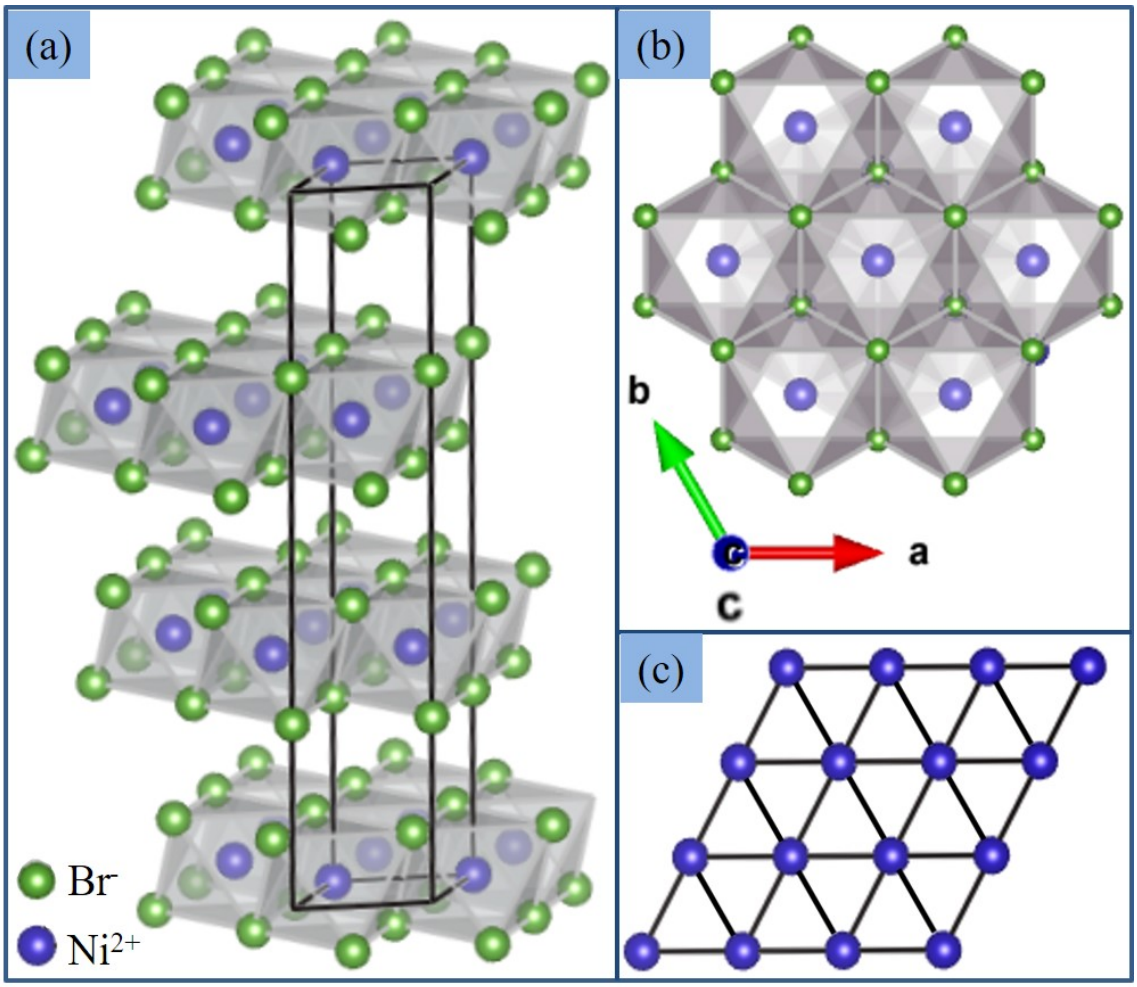

Fig. 3.1 (a) Schematic representation of $CdCl_2$ type crystal structure of $NiBr_2$. Blue & green sphere represent transition metal (Ni) and halogen (Br) ions, respectively. In Fig. (a), one formula unit cell of hexagonal crystal structure is outlined with a, b, and c are crystalline axis of the cell, where c is the axes of high-symmetry axis. (b) Atomic configuration for a layer of triangular lattice $NiBr_2$. (c) (a–b) basal plane representation of single layer of Ni^{2+} ions.

A triangular-lattice layer comprises edge-shared $NiBr_6$ octahedra (see Fig. 3.1(b)) and stacks along the high symmetry c-axis, where blue and green spheres correspond to Ni & Br ions, respectively. Each layer is bond with the others through weak van der Waals forces [140], and the (a–b) basal plan view of a single layer of cations (Ni) is shown in Fig. 3.1(c). Fig. 3.1(a, b, and c) are generated by VESTA software) [141].

3.3 Magnetic structure

Interest in such material is trigger by the study of low dimensional magnetism. $NiBr_2$ has long been studied as one of the prototypes of antiferromagnets with a triangular spin-lattice as shown in Fig. 3.2 (a), illustrating the spin arrangement in a single layer of transition metal which is ferromagnetic, and antiferromagnetically coupled on expanding along c-axis [64, 67, 68].

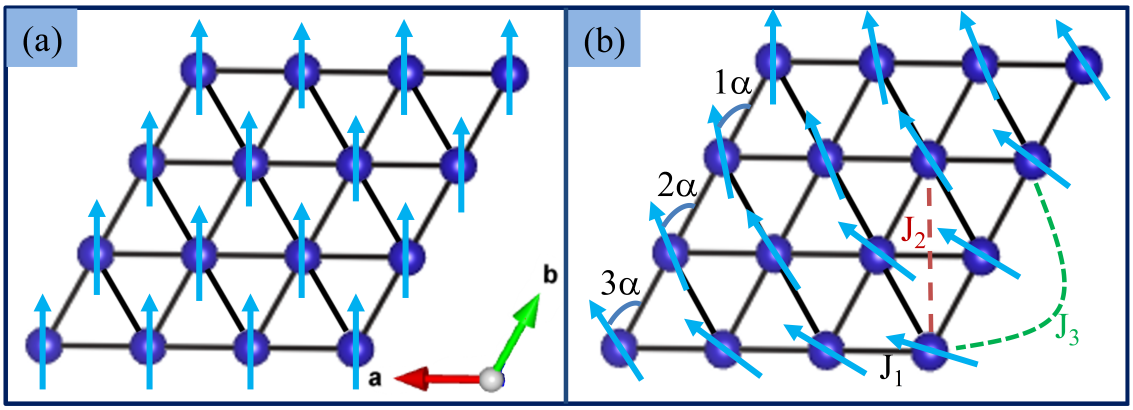

Fig. 3.2 (a) A typical representation magnetic structure of $NiBr_2$, demonstrating the collinear antiferromagnetic ($23K < T < 52K$), where blue spheres represent transition metal ions (Ni^{2+}) and solid arrows show the spin directions of nickel ions. (b) Helimagnetic ($T < 23K$) spin structures in (a–b) basal plane with defined exchange interaction coefficients. $J_{1,2,3}$.

At low-temperature bellow $23K$, $NiBr_2$ shows the noncollinear spin structure, and each ferromagnetic layer becomes helimagnetic in (a–b) basal plane and forming the spiral structure [131–133, 142] on stacking the layers along c-axis as shown in Fig. 3.2(b). Below helimagnetic transition, the magnetic moments aligned incommensurately helimagnetic structure with the periodicity that varies with temperature and applied field. At $T = 4.2$ K, the helimagnetic angle (α) close to 10°, and the magnetic moments are lying within the basal plane for $NiBr_2$ [139, 143, 144]. The propagation vector of this structure is (0, 0, 3/2). Below the transition temperature T_{IC}, the spins are rotated with a propagation vector (γ, γ, 3/2), giving a helix structure. As the hexagonal layer in the (a–b) basal plane is illustrated in Fig. 3.2(b). Both the magnetic structures are shown in Fig. 3.2(a, b) are differ by the parameter γ, which is zero in the antiferromagnetic phase, takes the value 0.027 in the helical phase at temperature $4.2K$, and then decreases as increasing the temperature up to $23K$, and vanishes beyond this value of temperature [139, 143]. The helimagnetic angle (α) is related to the parameter γ by $\alpha = 2\pi\gamma$, which is shown in Fig. 3.2 (b).

Magnetism in the $NiBr_2$ insulating transition metal dihalide compound is expected to be spin angular momentum (S) only, as orbital momentum (L) vanishes in this configuration. So, total angular momentum ($J = L + S$) implies $J = S$] associated with the partially filled d orbitals [140]. Noncollinear spin arrangements in helimagnets are often resulting from the presence of competing for ferromagnetic and antiferromagnetic Heisenberg interactions between spins in a geometrically frustrated magnet [61, 145]. Various microscopic driving mechanisms would yield noncollinear spin ordering, and among them, Dzyaloshinskii-Moriya interaction (DMI) is the most common and studied for various materials systems [7, 8].

Noncollinear spin arrangements in helimagnets are often result from presence of competing ferromagnetic and antiferromagnetic Heisenberg interactions between spins in a geometrically frustrated magnet [25]. $J_1 - J_3$ $(J_1 - J_2)$ model in a magnetic field of intensity H, the Hamiltonian ($\boldsymbol{H}$) for such triangular-lattice can be express through following Eq. (1))-

$$\boldsymbol{H} = -J_1 \Sigma_{<i,j>} S_i . S_j - J_{2,3} \Sigma_{<<i,j>>} S_i . S_j - H \Sigma_i S_i \tag{3.1}$$

where $\Sigma_{<i,j>}$ and $\Sigma_{<<i,j>>}$represent the sum over the nearest-neighbor (nn) and third nearest-neighbor (nnn), respectively [25]. With only nn interaction, which is antiferromagnetic in nature, the ground state of such a system is commensurate to the adjacent lattice. However, on the other hand, the competing interactions such as $J_1 > 0$ and the AF third-neighbor interaction $J_3 < 0$ with $J_1|J_3| < 4$ an incommensurate ground state appears [25, 26]. In other words, when nnn interaction becomes dominant, the ground state often results in an incommensurate spiral structure [25, 26, 61, 62]. In such a compound, the magnitude of the antiferromagnetic nnn interaction is larger than the ferromagnetic nn interaction. In the presence of an external applied magnetic field, the ordered state of the sublattices structure robust and leads to an exciting phase diagram as a function of temperature [25, 26, 61, 62].

3.4 Experimental details

Excellent quality of single crystals of $NiBr_2$ was grown at the University of Amsterdam by utilizing a self-flux growth approach starting from a stoichiometric ratio of Ni and Br, and followed by air-sensitive heat treatments as per details stated earlier [67, 68, 146]. The obtained single crystals are grown clearly in a layered form that efficiently cleaves along the c-axis. The samples have been studied with an average weight of 10 milligrams. The

measured single crystals had typical dimensions of approximately $4 \times 4 \times 2$ mm^3. $NiBr_2$ crystals are hygroscopic in nature; therefore, they are kept in a vacuum to prevent any degradation of the sample's quality. The low-temperature bulk magnetic measurements were performed for the temperatures in the range of 5 K to 250 K and applied field strength up to $H = 3\ T$ parallel to (a–b) basal plane on single-crystal $NiBr_2$, using the MPMS ®3 device (Quantum Design Inc.) system. M-H loop measurements were also carried out using the MPMS at various temperatures with an applied magnetic field up to $\pm 3T$ perpendicular to the c-axis. Special attention had been given towards the low temperatures, in the range of 5K to 60K. The magnetic hysteresis loops were recorded across transitions in order to better understanding of spin ordering. Differential magnetic susceptibility $dM(H)/dH$ data has been extracted. The magnetic measurements have been conducted on the samples that were fixed to quartz sample holders using diamagnetic glue.

3.5 Results and discussion

3.5.1 Structural characterizations

The internal morphology of the $NiBr_2$ nanoparticles was investigated by TEM. Fig. 3.3(a) shows the transmission electron microscopy (TEM) data of $NiBr_2$ powder sample followed by ultrasonication in ethanol medium for 1 hr, which show that $NiBr_2$ exhibits nearly spherical morphology with average particle size 5 nm. The SAED pattern shown in Fig. 3.3(b) corresponds to the TEM data shown in Fig. 3.3(a), showing the polycrystalline nature of the $NiBr_2$ powder sample. Whereas Fig. 3.3(b) shows the SAED pattern; the marked planes are theoretical in good agreement with that of reported data [67, 68, 146].

3.5.2 dc magnetization

Fig. 3.4 shows the temperature dependence of magnetization measurement for various magnetic field values (H), ranging from 0.1– 3.0 T, which is applied in the (a-b) basal plane. It is clearly evident that there are two distinct transitions in low-temperature regions, namely paramagnetic to antiferromagnetic transition at ($T_N \simeq 52K$) and antiferromagnetic to helimagnetic phase at ($T_{IC} \simeq 23K$), in vicinity of these transitions detailed neutron studies are demonstrated in Chapter 4. M-T data shows the different values of T_{IC} as a function of the applied magnetic field that suggests the non-collinear nature of spins below the T_{IC}. This non-collinearity arises due to competitive exchange interactions along with magnetic anisotropy in the triangular spin-lattice of helimagnet $NiBr_2$.

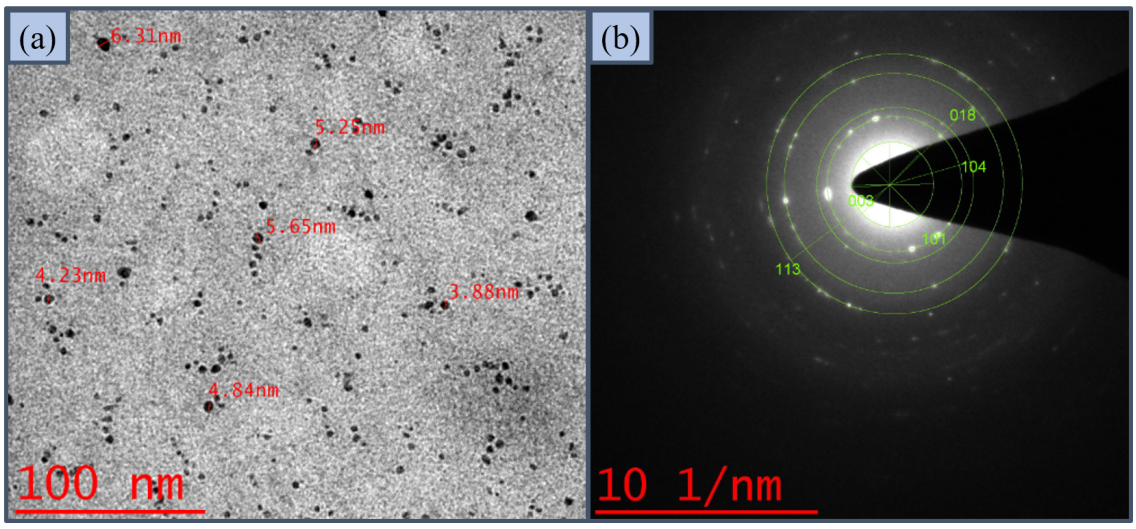

Fig. 3.3 TEM data analyses of $NiBr_2$ powder sample dispersed in ethanol. (a) TEM micrograph of $NiBr_2$ representing the nano particles, having average size 5nm. (b) shows the SAED pattern of nano particles obtained corresponding to Fig. 3.3 (a)

A closer inspection reveals that helimagnetic transition temperature T_{IC} decreases monotonically as the field increases. This demonstrates that T_{IC} is a highly field-dependent transition, whereas T_N shows a field independent collinear antiferromagnetic nature of spins.

Fig. 3.5 shows the M-H hysteresis loops measured at various temperatures ranging across 5-80K. At higher temperatures, the magnetization is linearly proportional to the applied magnetic field, as shown in the upper inset of Fig. 3.5.

Whereas at low temperatures, especially below T_{IC}, M is directly proportional to the field, i.e., shows antiferromagnetic nature up to a certain value of field ($\simeq 1T$), and beyond this value of a field, the linearity vanishes and an opening in the hysteresis appears, as shown in the lower inset of Fig. 3.5. These experimental findings are very much corroborating the M-T measurements data, as shown in Fig. 3.4. The lower inset in Fig. 3.5 shows the non-collinear incommensurate spin above the moderate value of field [133], which is marked in the magnetic phase diagram of $NiBr_2$ in the upcoming section.

Fig. 3.6 illustrates the temperature dependence of the dc magnetic susceptibility $\chi = M/H$ of $NiBr_2$, where the M is the magnetization, and the H is the magnetic field between 0.1 T and 3 T applied perpendicular to the c-axis. It is evident that $\chi(T)$ is the field independent of temperatures above 80 K. At low temperatures, two well-distinguished anomalies can be discerned marking magnetic phase transitions corresponding to collinear antiferromagnetic at nearly 45K and helimanetic at 23 K.

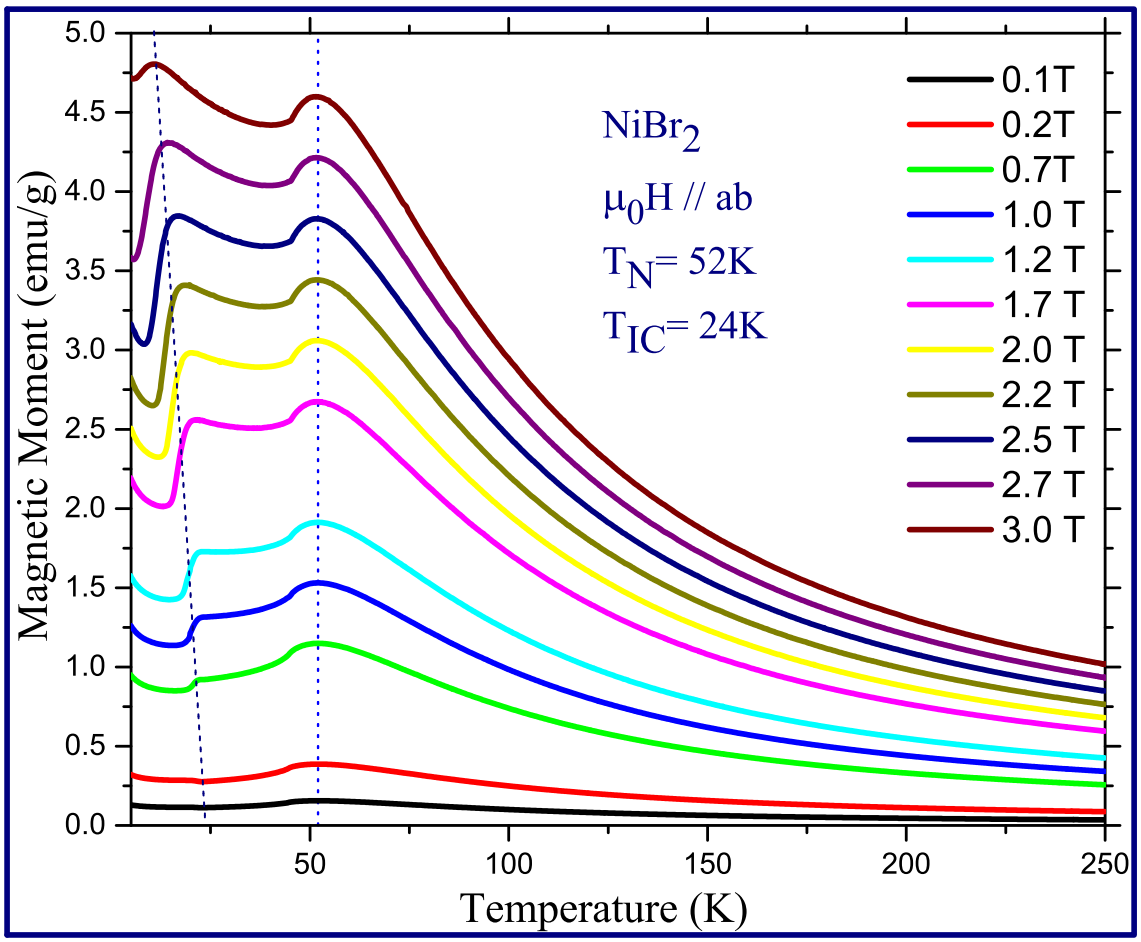

Fig. 3.4 Temperature dependence of magnetization on single crystal $NiBr_2$ measured for various values of applied field in (a–b) basal plane.

3.5.3 Differential magnetic susceptibility

The magnetization measurements (Fig. 3.4 & 3.5) allow us to determine the differential magnetic susceptibility, dM(H)/dH numerically by differentiating the dc magnetization data, as shown in Fig. 3.7.

For higher temperatures, it is evident that the derivative of magnetization is totally independent within field range ±3T. Whereas, at the low temperatures below 25K, the formal the scenario is ruled out, and a high dependency on temperature is observed, *i.e.*, dM(H)/dH is highly consistent with the helimagnetic nature of spin for the given direction of the field. At higher temperatures (above 80K), there is an absence of any ordering that shows the paramagnetic behavior of the sample, *i.e.*, there is no significant change in the rate of magnetization with respect to the applied magnetic field. The experimental

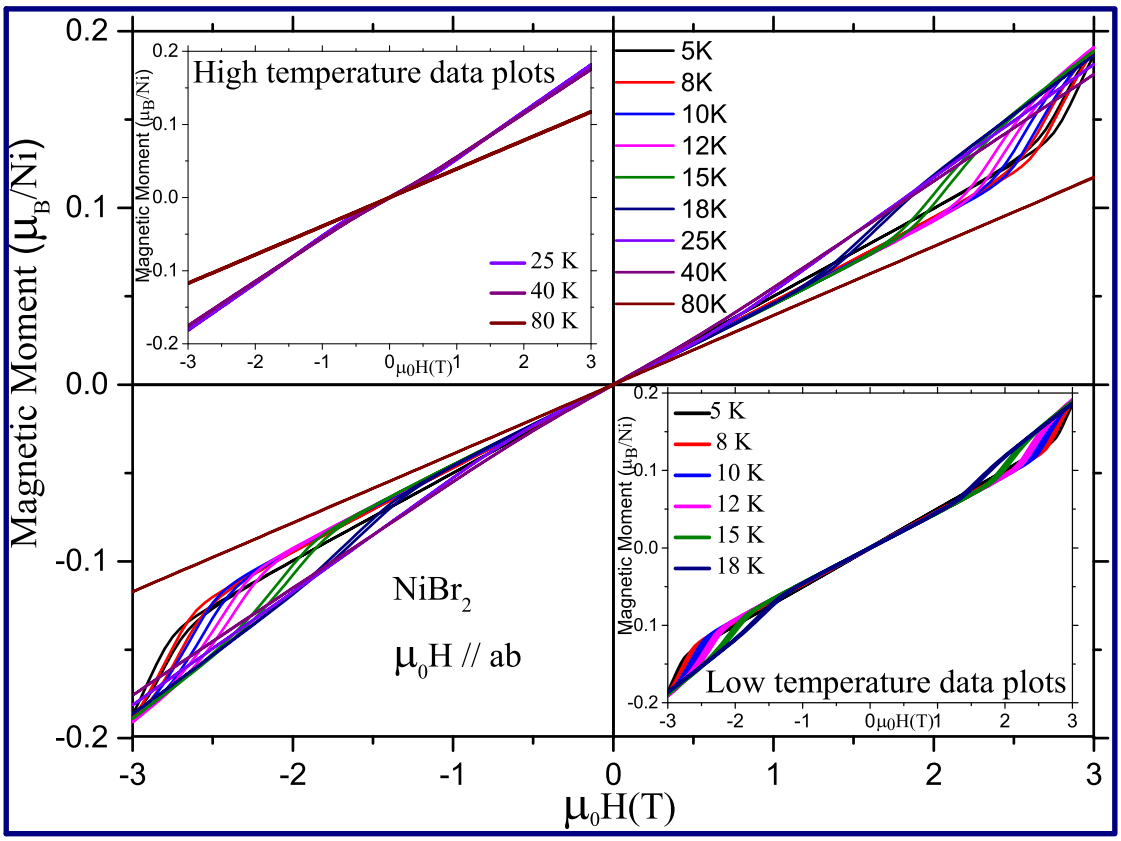

Fig. 3.5 Magnetization versus magnetic field for single crystal $NiBr_2$ at various temperatures. The field dependence of magnetization for low and high temperatures are shown in the inset Figs. in the field range $\pm$3T $\perp$ c-axis.

investigations on single-crystal $NiBr_2$ confirm the reorientation of spins and the evolution of non-collinear incommensurate spin structures at low temperatures and above a definite value of the applied magnetic field [60].

Fig. 3.8 shows the relative comparison between χ_{dc} and χ_{ac}, and both are measured H_{dc} = 2 kOe. The related temperature derivatives are depicted in the inset of Fig. 3.8 The measurement of χ_{ac} assures precise determination of the temperature of the long-range magnetic ordering $T_{N,m}$. $T_{N,m}$ may be determined from the χ' maximum or the $d\chi'/dT$ minimum. Usually, the temperatures of $d\chi'/dT$ minimum and of χ/dT onset coincide, which is the case also here. The field and temperature dependence of the ac-susceptibility near 20 K are more complicated; this reflects several complex phase boundaries, from both dM(H)/dT and dM(H)/dH are in close proximity, if not coincident, here. In this region, the ac-susceptibility peak amplitudes first increase before decreasing again with for various dc-field. In contrast, the susceptibility peak temperatures increase monotonically with the field, tracking closely along the phase boundaries across T_m regimes determined from

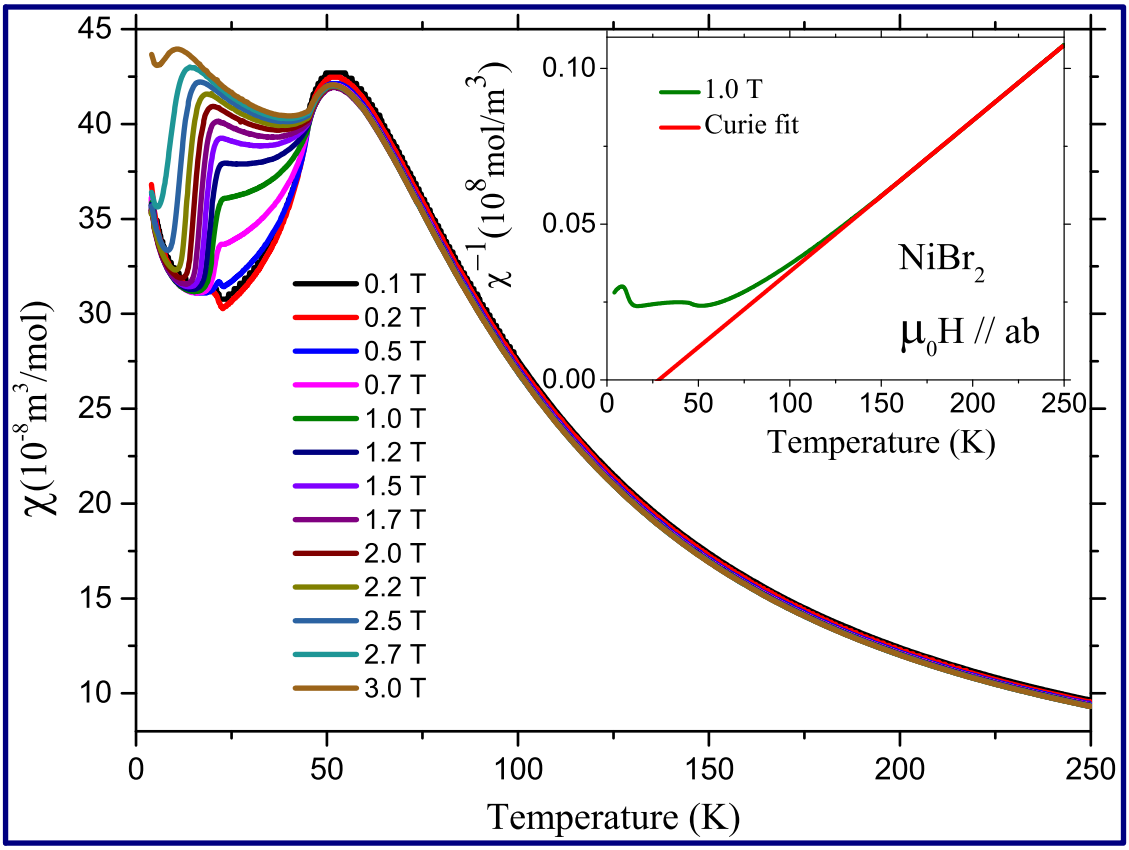

Fig. 3.6 Temperature dependence of magnetic susceptibility for $NiBr_2$ single crystal measured with field applied parallel to (a–b) basal plane. The inset shows the temperature dependence of the inverse magnetic susceptibility $1/\chi(T)$ measured at 1 T is shown.

dM(H)/dT and dM(H)/dH estimates. Furthermore, the ac susceptibility peak temperature-field profile over the 'atypical' regime maps directly onto the field-induced modulation in the incommensurate phase. It should be noted that the zero-field ac-susceptibility falls monotonically with increasing temperature between 5 and 20 K. On the basis of the argument that the uniform applied field is the conjugate field for a collinear magnetization, one might initially anticipate that the ac susceptibility (peak) would display a monotonic variation with field along with the entire low-temperature phase. The ac-susceptibility peak falls with the increasing field on exiting the incommensurate phase, which is reminiscent of the case for conventional antiferromagnetic to helimagnetic transition. This behavior in $\chi_{ac,dc}(H,T)$ may be a defining characteristic of such transitions, specifically reflecting the combination of ferromagnetic and antiferromagnetic interactions in the triangular $NiBr_2$ system that leads to the complicated influence of applied fields on the changing spin configurations across the incommensurate phase.

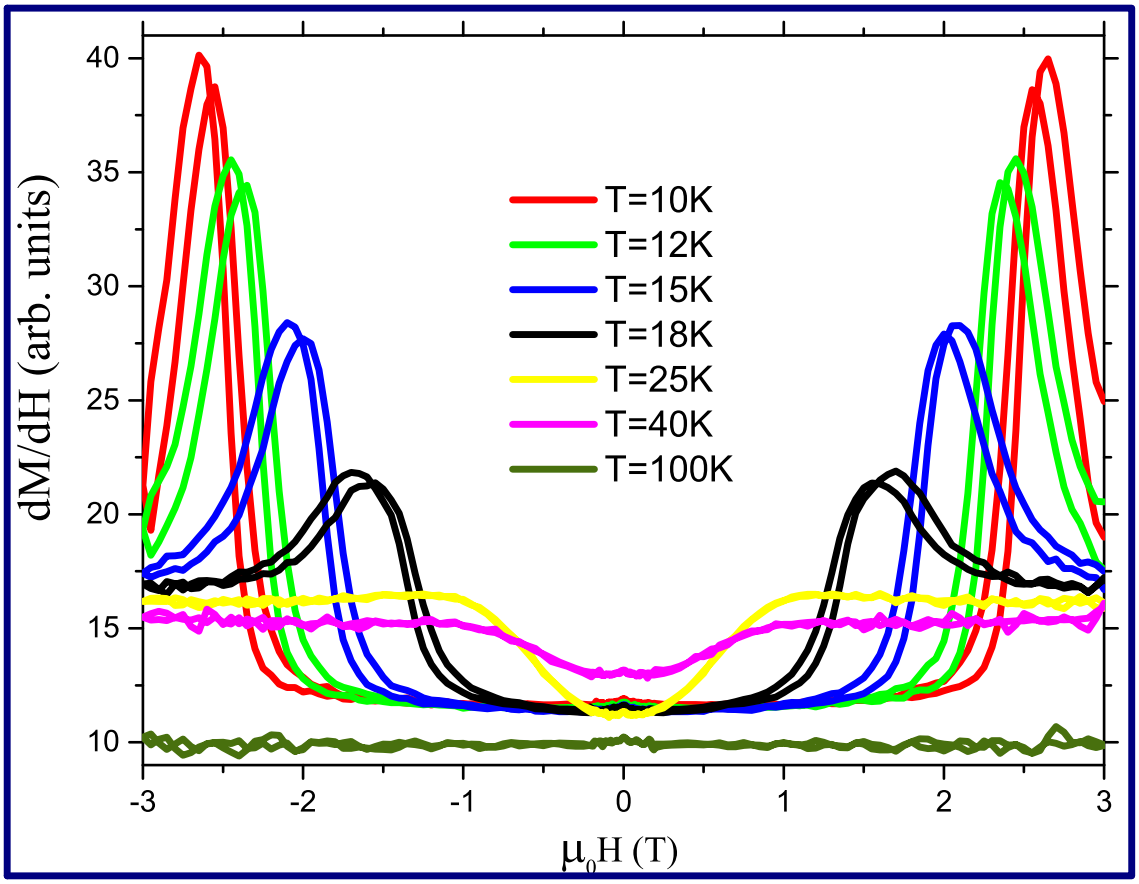

Fig. 3.7 Differential magnetic susceptibility dM(H)/dH vs. magnetic field, H measured in the (a-b) basal plane for various temperatures lying in the range of 10-100K.

The temperature dependence of magnetic susceptibility $\chi_{ac,dc}$ of $NiBr_2$, and the first derivative of the $\chi_{ac,dc}$ is shown in the inset of Fig. 3.8. The $\chi_{ac,dc}$ of the sample exhibits a broad maximum close to T_{max} = 15 K, while the derivative dχ/dT shows a sharp peak very proximal to each other at magnetic field 2T applied in (a–b) basal plane. Closer inspection reveals the significant shift in ac & dc magnetic susceptibility maximum in magnetic susceptibility is a signature of transformation from the collinear antiferromagnetic to the noncollinear modulated incommensurate structure [68, 147].

3.5.4 Magnetic phase diagram of $NiBr_2$

The magnetic phase diagram of $NiBr_2$ as a function of field/temperature has been inferred from the dc magnetometry. The entire temperature range studied can be subdivided into three regions with decreasing T (see Fig. 3.9).

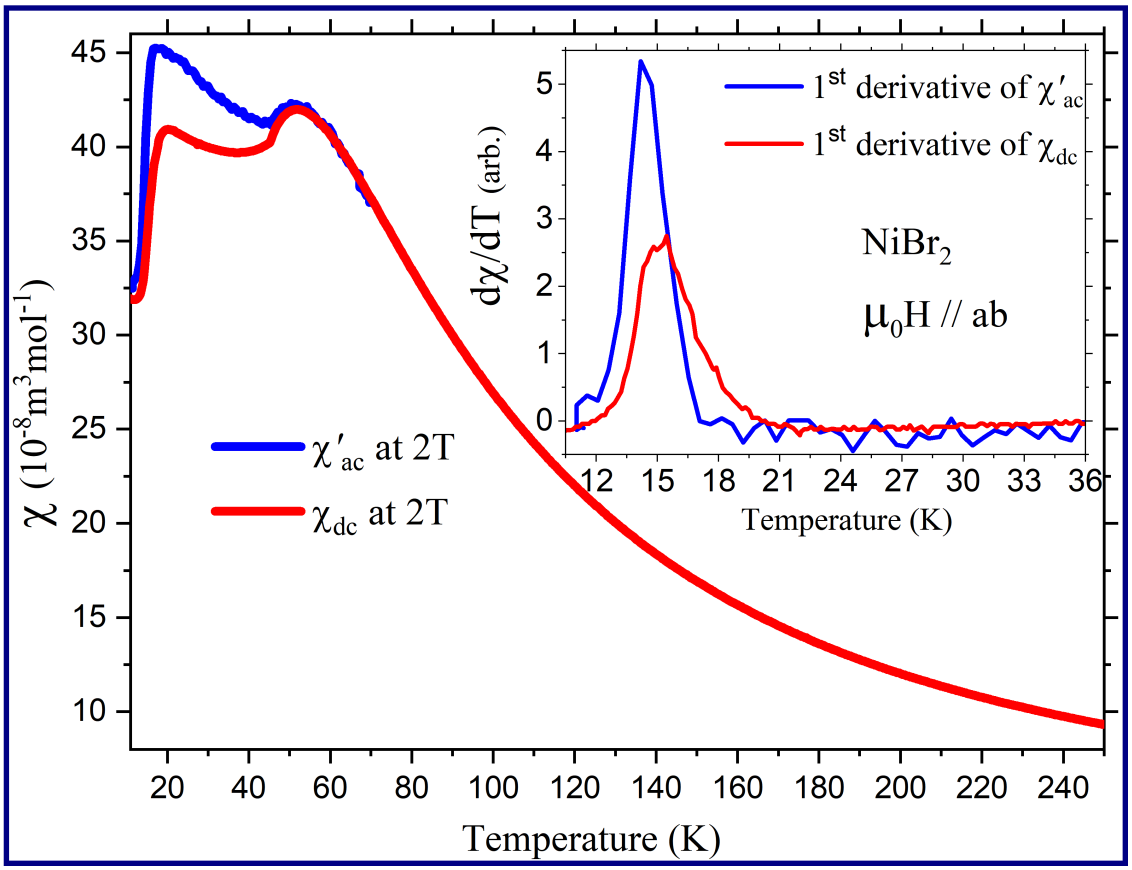

Fig. 3.8 Relative variation of temperature dependence of ac(dc) magnetic susceptibility for $NiBr_2$ single crystal measured with field applied parallel to (a–b) basal plane. The inset shows the temperature dependence of first order derivative of magnetic susceptibilities w.r.t. temperature at $2T$ magnetic field applied in (a–b) basal plane.

At the high-temperature side in the first region (T>52 K), $NiBr_2$ shows a predictable paramagnetic behavior. In the second region ($T_N \leq$ T $\leq$ 23 K), *i.e.*, the intermediate region, $NiBr_2$ exhibits both the properties: predictable anti-ferromagnetic ordered and partially paramagnetic responses. As we decrease the T further below T_{IC} = 23 K in the third region, the incommensurate helical phase evolves [132]. These asterisk and triangular dashed-lines in the H-T diagram are an extrapolation. As one can notice, a clear field-induced transition occurs beyond the critical value of field ($\simeq 3.5T$) and incommensurate spin-spiral phase disappears (as shown in the H-T diagram of $NiBr_2$). As a result, $NiBr_2$ exhibits a clear field/ temperature-induced incommensurate to commensurate phase transition.

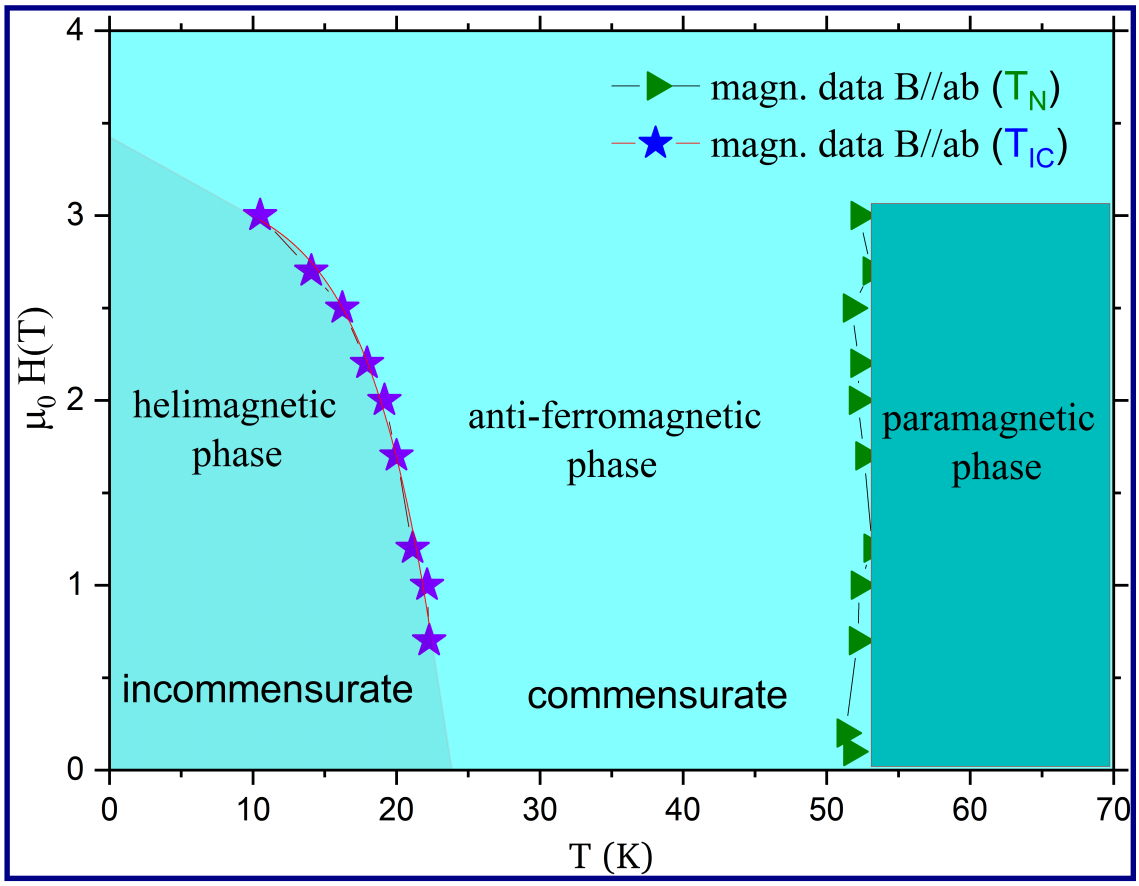

Fig. 3.9 Magnetic phase diagram of $NiBr_2$ constructed from magnetization measurements, stars and triangles represents different regimes corresponding to T_{IC} and T_N, respectively.

3.6 Conclusions

In conclusion, the non-collinear magnets are promising series of multi-functional materials that show vast technological applications in next-generation ultra-dense and energy-efficient data storage devices. Here, by utilizing the magnetization measurements and differential magnetic susceptibility, the magnetic phase diagram of $NiBr_2$ was extracted. The external magnetic field, H || (a-b) basal plane were applied, and compared the results with the previous investigations, which are well in agreement. The entire temperature range studied can be subdivided into three regions. The higher temperature regimes (above 52 K) correspond to the paramagnetic phase. Upon decreasing the temperature, antiferromagnetic commensurate phase between 23-52 K, and below 23 K, a helical incommensurate phase is identified in the H-T diagram. A closer inspection of the applied field in both transition regions interestingly shows that the helimagnetic phase disappears beyond a critical field value ($\simeq 3.5T$). In contrast, the antiferromagnetic transition is independent of the value

of the applied magnetic field. The fact indicates a magnetic field-induced transition from non-collinear to collinear state. These findings have high relevance for next-generation ultra-dense data storage devices, especially in spintronics.